Technical Assessment of the Joint CSIRO/Bureau of Meteorology Proposal for a Geostationary Imager/Sounder over the Australian Region

D. M. O'Brien and R. M. Mitchell

DIVISION OF ATMOSPHERIC RESEARCH TECHNICAL PAPER No. 15

COMMONWEALTH SCIENTIFIC AND INDUSTRIAL RESEARCH ORGANISATION, AUSTRALIA 1987

Technical Assessment of the Joint CSIRO/Bureau of Meteorology Proposal for a Geostationary Imager/Sounder over the Australian Region

By D. M. O'Brien and R. M. Mitchell

Division of Atmospheric Research Technical Paper No. 15

Commonwealth Scientific and Industrial
Research Organisation, Australia
1987

National Library of Australia Cataloguing-in-Publication Entry

O'Brien, D. M.

Technical assessment of the joint CSIRO/Bureau of Meteorology proposal for a geostationary imager/sounder over the Australian region.

Bibliography.
ISBN 0 643 04285 7.

1. Remote sensing—Equipment and supplies. 2. Meteorological satellites. 3. Geostationary satellites. I. Australia. Bureau of Meteorology. II. Commonwealth Scientific and Industrial Research Organisation (Australia). Division of Atmospheric Research. III. Title. (Series: Division of Atmospheric Research technical paper; no. 15).

621.36'78

87.361–770

1.0 INTRODUCTION AND BASIC FINDINGS.

In April 1986 CSIRO and the Australian Bureau of Meteorology proposed a combined imager/sounder for geostationary orbit over the Australian region. This ambitious instrument, referred to as the Imaging Spectrometer and Atmospheric Sounder (ISAS) throughout this report, was to provide:

(1) visible imagery with high spatial and spectral resolution;

(2) infrared imagery with both high spatial resolution and low noise equivalent differential temperature (NEΔT) at 300 K;

(3) infrared sounding with low NEΔT.

In short, the ISAS instrument was to surpass the specifications of the CZCS, AVHRR and HIRS instruments from geostationary rather than polar orbit.

In this report the technical feasibility of the proposal is assessed. The principal findings and recommendations of the report are as follows.

(1) Visible imagery with spatial resolution of 500 metres and spectral resolution of 20 nm is possible with signal to noise ratios comparable to those predicted for GOES NEXT. If the spatial resolution is degraded to 1000m, then the signal to noise ratio is superior to CZCS imagery.

(2) Infrared imagery with spatial resolution of 2 km and noise equivalent differential temperatures less than 0.1 K is possible in the 2.2, 3.9 and 10 μm atmospheric windows.

(3) There are three viable options for the infrared sounder, namely, a conventional filter wheel radiometer, an interferometer, and a grating spectrometer. The performance predicted for the sounder should surpass that of the HIRS instrument presently flown on the NOAA series of polar orbiting satellites.

(4) Rough order of magnitude estimates for the size and weight of ISAS are 2000 x 860 x 860 mm and 365 kg. Consequently, ISAS will require a dedicated spacecraft, which also must be three-axis stabilised, rather than spinning, in order to provide adequate dwell times.

(5) ISAS appears to be technically feasible, although there are complex, unresolved problems associated with spacecraft stability and pointing accuracy of the telescope (Section 3.2).

(6) If international financial support is forthcoming, then the instrument outlined in this report warrants a technical phase A study.

2.0 SPECIFICATION OF ISAS.

A survey of the Australian remote sensing community, undertaken in early 1986, found that the future requirements of the community could be summarised as in Table 1.

TABLE 1. User requirements.

User group	Application	Specifications			
Meteorology	Sounding	NEΔT	<	0.2	K
	Visible imagery	Spatial resolution	<	2	km
		Spectral resolution	<	100	nm
	Infrared imagery	Spatial resolution	<	4	km
Oceanography	Sea surface temp	NEΔT	<	0.1	K
	Ocean colour	Spectral resolution	<	20	nm
		Spatial resolution	<	1	km
Hydrology	Surface temp	NEΔT	<	0.1	K
	H_2O profiles	Spatial resolution	<	2	km
Land use	Surface temp	NEΔT	<	0.1	K
	Surface colour	Spectral resolution	<	20	nm
		Spatial resolution	<	0.5	km

In addition, the survey found that:

(1) all groups favoured a geostationary instrument in order to free their observations from the specific times of overpass of the polar orbiting satellites;

(2) all groups indicated that a scan time of three hours for the full disc would be acceptable, provided that the instrument could be controlled from the ground to scan limited areas for measurement of 'cloud winds' and in times of severe weather or other emergency.

These broad requirements were translated into specific recommendations for the instrument channels in the original proposal, most of which have been retained in the present assessment.

There are several options possible for the sounder, such as a conventional filter wheel radiometer, an interferometer, and a grating spectrometer. However, it was assumed for the purpose of this assessment that the specifications for the sounder channels and their sensitivities would be the same as for the improved HIRS/2I instrument, scheduled to be flown on the next series of NOAA polar orbiting satellites. These specifications are listed in Table 2.

TABLE 2. Sounder channel specifications.

Channel #	λ	$\Delta\lambda$	$NE\Delta N$*
	μm	μm	mW m^{-2} sr^{-1} $(cm^{-1})^{-1}$
1	14.71	0.216	0.50
2	14.49	0.252	0.53
3	14.22	0.324	0.29
4	13.97	0.312	0.20
5	13.64	0.298	0.24
6	13.35	0.285	0.20
7	11.11	0.432	0.10
8	9.71	0.236	0.15
9	8.16	0.400	0.16
10	7.33	0.215	0.20
11	6.72	0.361	0.19
12	4.57	0.048	0.006
13	4.52	0.047	0.003
14	4.46	0.046	0.004
15	4.40	0.045	0.002
16	4.24	0.041	0.002
17	4.00	0.055	0.002
18	3.76	0.141	0.001
19	0.69	0.048	0.1% albedo

* $NE\Delta N$ denotes the noise equivalent differential radiance.

The infrared imager specifications, listed in Table 3, were chosen to give infrared imagery in the 2.2, 3.9 and 10 μm windows, with the latter window split in order to allow for corrections for water vapour in surface temperature observations. In addition, a channel at 6.7 μm was included to monitor atmospheric water vapour. A nominal resolution of 2 km was set for each channel, although subsequent calculations show that at 10 μm the telescope is diffraction limited and that a more realistic estimate of the resolution is likely to be 3 km.

TABLE 3. Infrared imager channel specifications.

Channel #	Wavelength range	Spatial resolution	NE$\Delta\rho$*	NEΔT	Scene temp
	μm	km	%	K	K
1	2.05 - 2.35	2	0.10		300
2	3.80 - 4.00	2		0.10	300
3	6.50 - 7.00	2		0.50	230
4	10.20 - 11.20	2		0.10	300
5	11.50 - 12.50	2		0.10	300

* Note that the noise equivalent differential albedo NE$\Delta\rho$ is specified for channel 1, rather than the noise equivalent differential temperature.

The requirement for the visible imager was to supply data similar to CZCS/GOES for oceanographers/meteorologists, and this led to the list of eight channels suggested in the original proposal. It was subsequently found that the 600 mm telescope proposed for ISAS would allow 500 m spatial and 20 nm spectral resolution throughout the whole visible spectrum, so the possibility of an imaging spectrometer was considered. Such a device allows all channels to share the same footprint and to be sampled simultaneously. The dispersive element for the spectrometer could be either a grating or a prism. The latter has the advantage that its energy efficiency is almost constant over the visible spectrum, but the disadvantage that its dispersion decreases with wavelength. Consequently, when used with a detector array whose pixel spacing is uniform, the placement of the channels of a prism spectrometer is controlled by the power of the prism, a fact which might not be acceptable to some members of the remote sensing community. Despite this potential difficulty, the channel centres and widths used in this report were calculated for the prism spectrometer described in Appendix 1 and are listed in Table 4.

The instrument packages of ISAS must have not only high precision, as specified above, but also high accuracy. Calibration targets and the frequency of observation of such targets are not discussed in this report, although the difficulties in designing targets with precisely controlled temperature/reflectivity are clearly recognised.

TABLE 4. Visible spectrometer channels.

Channel #	λ_{min} nm	λ_{max} nm	$\bar{\lambda}$ nm	$\Delta\lambda$ nm	Spec S/N at 1% albedo
1	400.0	410.9	405.5	10.9	20
2	410.9	422.5	416.7	11.6	20
3	422.5	434.8	428.7	12.3	20
4	434.8	448.0	441.4	13.1	20
5	448.0	462.0	455.0	14.0	20
6	462.0	477.0	469.5	15.0	20
7	477.0	493.1	485.1	16.1	20
8	493.1	510.5	501.8	17.3	20
9	510.5	529.2	519.8	18.7	20
10	529.2	549.4	539.3	20.2	20
11	549.4	571.2	560.3	21.9	20
12	571.2	595.1	583.1	23.8	20
13	595.1	621.0	608.0	26.0	20
14	621.0	649.5	635.3	28.5	20
15	649.5	680.8	665.2	31.3	20
16	680.8	715.5	698.2	34.6	20
17	715.5	753.9	734.7	38.5	20
18	753.9	796.9	775.4	43.0	20
19	796.9	845.3	821.1	48.3	20
20	845.3	900.0	872.6	54.7	20

3.0 TECHNICAL ASSESSMENT

A schematic of the proposed instrument is shown in Figure 1. The functions of the visible imager, infrared imager, and infrared sounder are separated in the focal plane of the telescope. This implies that the different instruments observe different footprints on the earth, as shown in Figure 2. This arrangement makes full use of the available energy and is a natural first choice, unless there is an overriding requirement for simultaneous observations by all three instruments (a task which would be difficult because the instruments have different resolutions). In the sections which follow, each of the components of the system will be discussed briefly.

3.1 Focal Plane Splitter.

Figure 1 is purely schematic, and in reality the distance between the images of the different footprints in the focal plane is large in comparison with the images, as shown in Figure 3. Separation of the footprints requires a device such as that shown in Figure 4. It consists of a prism, whose plane faces reflect light to the infrared instruments, and through which a conical hole has been bored to pass light to the visible spectrometer. Such a device maintains a fixed relationship between the reflected beams, a fact which might simplify the alignment of the instrument packages.

3.2 Scan Mirror.

As will be shown later, there is sufficient energy available with a 600 mm diameter telescope to give 500 m resolution in the visible with spectral channels only 20 nm wide. The quest for 500 m resolution places severe constraints on the stability of the spacecraft, and almost certainly would require a computer controlled scanning system which would sense fixed stars and compensate for the wobble of the spacecraft and the motion of components in other instrument packages. Such a system is being devised by ITT and Ford Aerospace in order to achieve 1 km resolution for GOES NEXT.

If pointing accuracy of 500 metres (14 μrad) is to be achieved, the instrument and the satellite must be considered as a whole. This presupposes a high level of cooperation between the instrument builder and the spacecraft manufacturer, and adds significantly to the cost of the project.

Before considering the design and fabrication of the scan mirror proposed for ISAS, it is worth considering the scan mirror for GOES NEXT (Table 5), the design of which is one of the more challenging aspects of the GOES NEXT program.

The scan mirror of GOES NEXT will receive direct sunlight onto part of the mirror near local midnight, so large thermal gradients of the order of 5 C will be produced in the mirror. Because the nickel coating and the beryllium base have different coefficients of thermal expansion, the temperature gradients lead to a warping of the mirror and consequent loss of pointing accuracy. Over the period of a day, the mirror temperature is expected to vary from 10 C to 30 C.

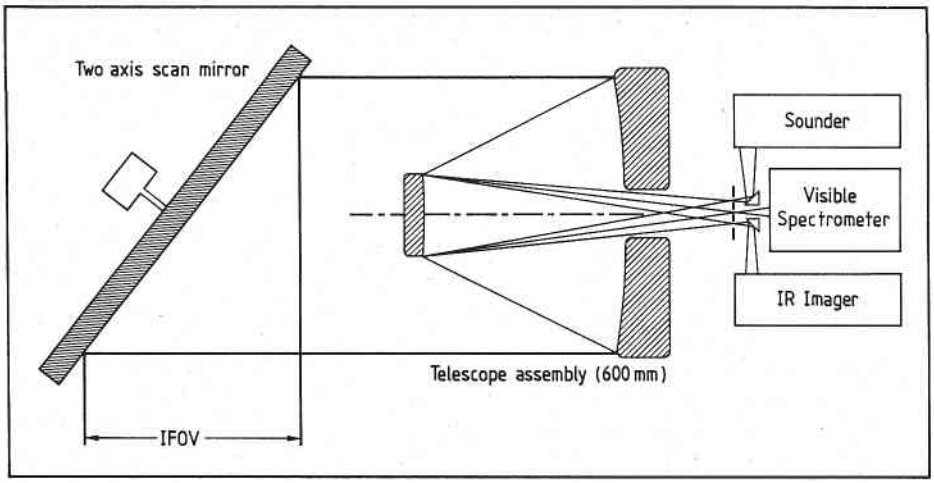

Figure 1: Schematic diagram of ISAS.

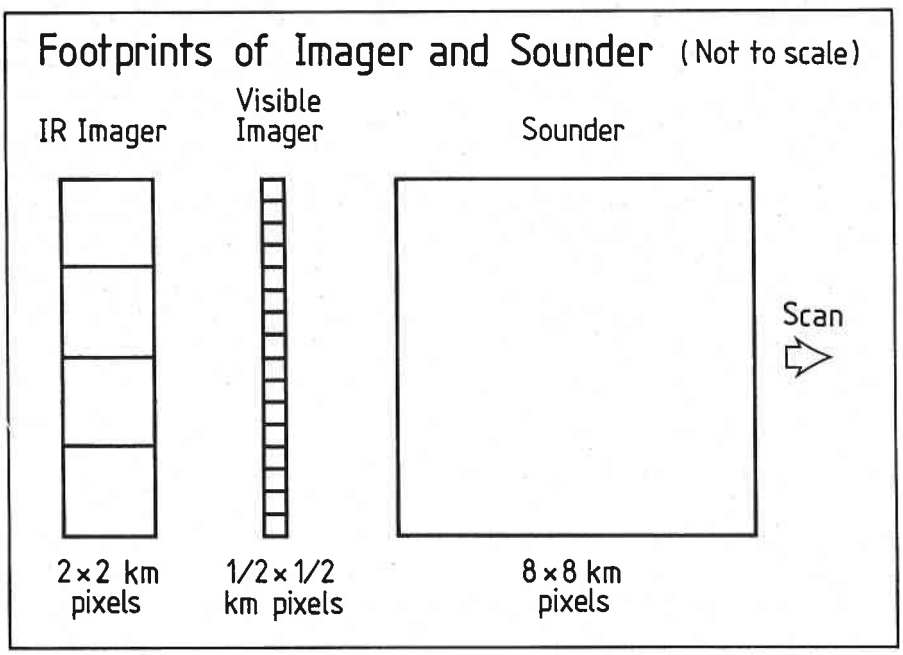

Figure 2: Footprints of the imagers and sounders, not drawn to scale.

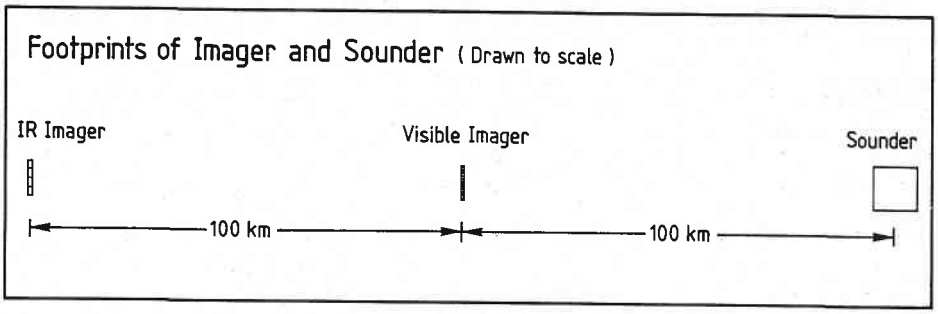

Figure 3: Focal plane of the telescope, drawn to scale.

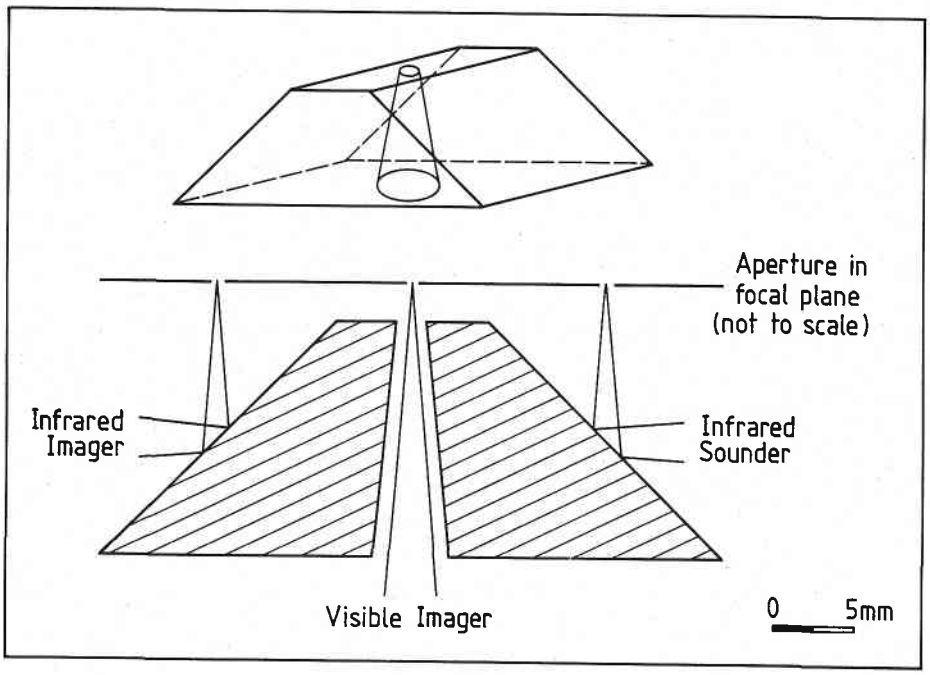

Figure 4: Prism beam splitter.

TABLE 5. GOES NEXT scan mirror.

Shape	Elliptical.
Size	Minor/major axes of 300/425 mm.
Weight	2 kg.
Material	Solid beryllium blank,
	nickel coating for polished surface,
	milled out from the rear,
	matte black on reverse of mirror surface,
	gold plating on ribs.
Drive	Two axis inductosyn drive.

While there is probably no great problem in producing a scan mirror of the size required by ISAS (minor/major axes of 600/850 mm), especially if hot isostatic pressing (HIP) is used to fabricate the mirror from beryllium powder, the thermal problem will be acute, because the magnitude of the warping probably will be twice that of GOES NEXT, whereas the pointing requirement is twice as precise.

If it is assumed that the footprint pattern of Figure 2 needs to be repeated 4 times in order to achieve a realistic signal to noise ratio for ISAS, then the scan rate for the mirror is approximately 30 seconds per line, or 2/3 degree per second. In addition it would probably be necessary to have a rapid scanning mode, so that the mirror could be swept aside to view space for calibration or directed to a limited area scan. Since the mirror mass would be at least 8 kg (estimated on the basis of the mirror for GOES NEXT), such rapid motions would have to be taken into account for the angular momentum budget of the satellite.

3.3 Telescope Design.

Preliminary calculations indicate that an f/5 Cassegrain telescope would have acceptable obscuration factor and blur diameter for the field of view required (3 mrad), as shown in Figures 5 and 6. Also shown for comparison in Figure 7 is an f/2.5 design, in which sufficient back focus has been allowed both for mechanical support and for placement of the secondary instrument packages. It is clear that the f/2.5 design is unacceptable, because the (linear) obscuration has reached 50%. In all calculations which follow, a focal ratio of f/6 has been assumed.

The prime mechanical requirements are light weight and thermal stability. Consequently, beryllium is a natural choice for the mirrors. Carbon fibre materials might well be suitable for the structural members, if the problems associated with creep and water absorption can be overcome. Carbon fibre has been used on the thematic mapper of LANDSAT, but special procedures were required to continually monitor the variations in the telescope length prior to launch.

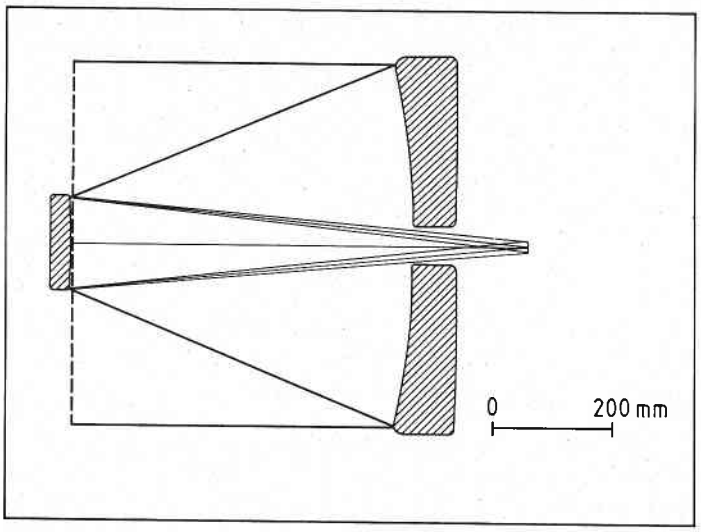

Figure 5: Scale diagram of an f/5 telescope.

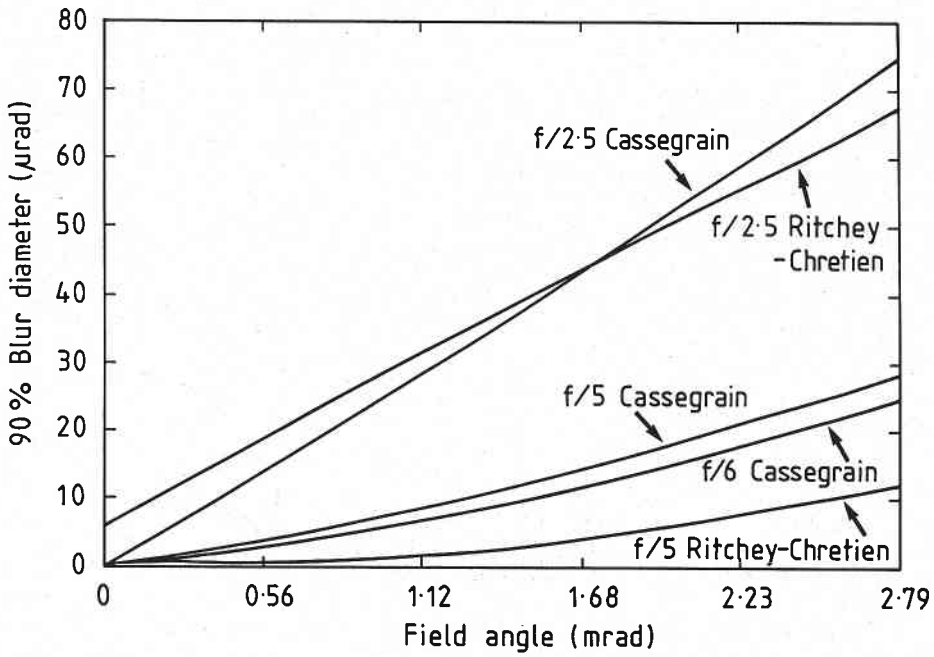

Figure 6: Blur diameters as a function of field of view.

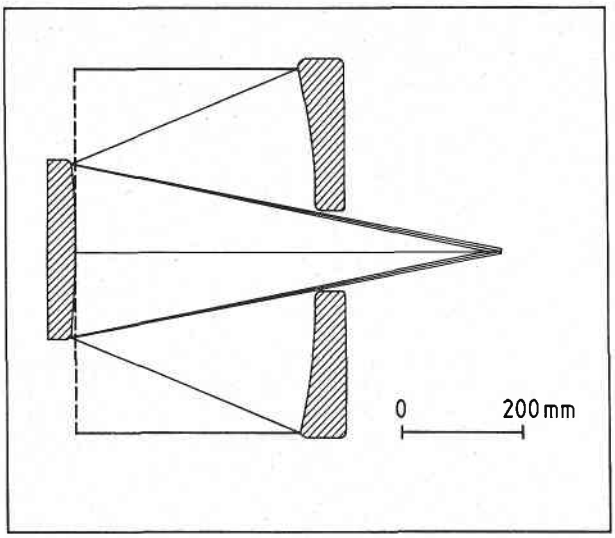

Figure 7: Scale diagram of an f/2.5 telescope.

Both GOES NOW and LANDSAT (built by Hughes Aircraft Company) have focus and alignment controls. On GOES NOW, the focus may be controlled from earth while the satellite is in orbit, whereas on LANDSAT the adjustment is only used while the instrument is in a simulated space environment in the laboratory. The proposal for ISAS has the field stop for each instrument in the focal plane of the telescope, rather than at the detector, so the alignment of the instrument packages will be critical. Consequently, a focus and alignment control would almost certainly be necessary in the laboratory, and possibly also necessary in space.

It is worth nothing that MATRA proposed a 600 mm, f/6, Ritchey-Chretien telescope for the next generation of METEOSAT. Separation of imager and sounder channels was to be achieved in the focal plane, so that not only did the separate instruments observe different footprints on the ground, but so too did the several channels of each instrument. [It seems that MATRA proposed to scan the field of view with a small mirror aft of the secondary telescope mirror. Calculations by CSIRO showed that this proposal leads to absurdly large blur diameters for footprints far from the optic axis. Consequently, such a scheme was not contemplated for ISAS.]

3.4 Visible Imager.

The number of channels requested by the user community is so large that the most practical approach is to analyse the visible and near infrared spectrum with an imaging spectrometer. A nominal resolution of 20 nm can be achieved comfortably with a narrow angle prism and 25 mm optics, as shown in Appendix 1. However, there are two questions which ought to be referred to the user community if a spectrometer is to be considered.

(1) In a spectrometer with a rectangular detector array, the placement of the spectral bands is fixed by the dispersion of the prism and the size of the pixels. Consequently, the spectrometer must offer sufficient spectral resolution over the whole visible spectrum that the user can synthesise the bands he requires from the data acquired. For users who require only broad band data (greater than 100 nm bandwidth), the nominal 20 nm resolution assumed in this study should be quite adequate. However, for users who require narrow bands (less than 100 nm bandwidth), the possibility that the band will not be centred at a specified wavelength must be considered. This point will be particularly important to oceanographers, since CZCS data have a half-power bandwidth of 20 nm. One obvious remedy is to sacrifice signal to noise ratio in order to increase the resolution of the spectrograph.

(2) The dispersion by a prism decreases from blue to red, although the dependence upon wavelength can be minimised with composite prisms fabricated from suitable glasses. Nevertheless, the dispersion at 400 nm would be at least four times the dispersion at 900 nm. Whether such a varying resolution could be accepted by the user community must be ascertained.

These points are illustrated by Figures 8 and 9 which show the placement of the channel centres and the channel widths for a prism spectrometer which spans the visible spectrum from 400 nm to 900 nm with 20 channels. The channel width is nominally 20 nm at 540 nm, but in fact varies from 11 nm at 400 nm to 54 nm at 900 nm. These channels, also listed in Table 4, have been used in the sensitivity analysis.

Both the problems mentioned above can be solved simply if the detector array is fabricated with non-uniform spacing of the elements in the spectral dimension. This is not technically difficult, but would add very significantly to the cost of the spectrometer package.

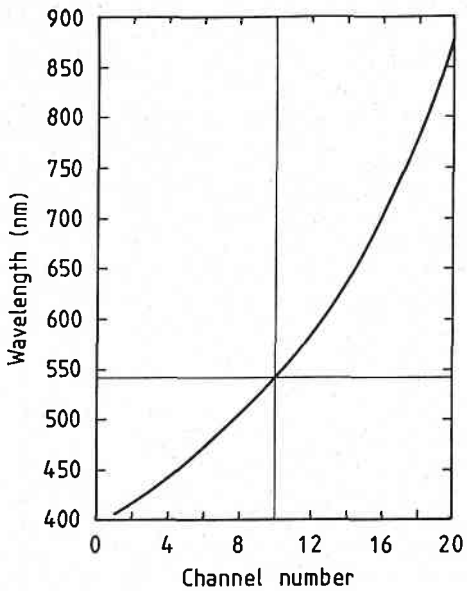

Figure 8: Visible spectrometer channel centres.

Sensitivity analyses for the visible spectrometer are contained in Appendix 2. They assume that the two dimensional photo-diode array is bump-bonded to an array of transimpedance amplifiers with multiplexed outputs. With such an array, the signal to noise ratio of each element is essentially that of an isolated diode and amplifier. The primary noise sources are the Johnson noise in the parallel dynamic resistance of the diode and feedback resistance of the amplifier, shot noise in the diode, and noise in the amplifier, although the last source should be neglible for state of the art amplifiers.

Two separate calculations were carried out, corresponding to the high/low albedo of land/sea with spatial resolutions of 0.5/1.0 km. They are summarised in the Tables 6 and 7.

TABLE 6. Land imagery at 560 nm.

	ISAS	GOES NEXT
Spatial resolution	0.5 km	1 km
Spectral resolution	22 nm	100 nm
S/N at 100% albedo	> 560	420
Dynamic range*	912	650

* Dynamic range is the ratio of the detector current at 100% and at 0% albedo.

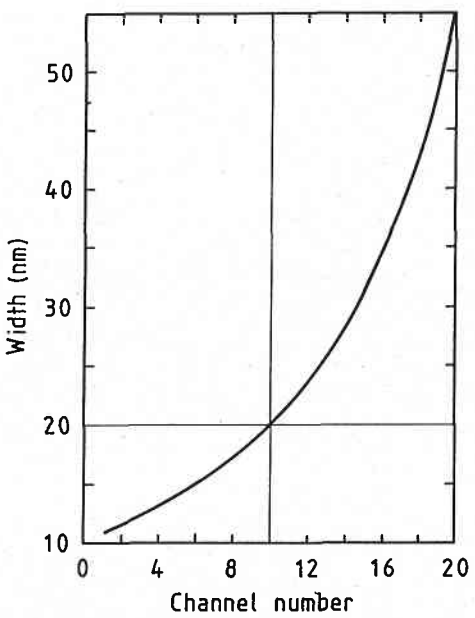

Figure 9: Visible spectrometer channel widths.

TABLE 7. Ocean imagery at 560 nm.

	ISAS	CZCS
Spatial resolution	1 km	0.825 km
Spectral resolution	22 nm	20 nm
S/N at 5.2% albedo	164	> 125
Dynamic range*	3648	limited by digitiser

* See footnote for Table 6.

Note that the albedo specified in the second Table corresponds to a radiance of 28.6 Wm^{-2} sr^{-1} $(cm^{-1})^{-1}$, the value used in the specification of the CZCS instrument.

The calculations show that:

(1) imagery superior to AVHRR and GOES NEXT is possible with a spectral bandwidth of 20 nm and spatial resolution of 0.5 km;

(2) the high signal to noise ratio of CZCS imagery can be achieved with a spatial resolution of 1.0 km, but not 0.5 km.

It is not possible to improve the signal to noise ratio by widening the swath to increase the dwell time without simultaneously increasing both the 1/f noise in the sounder and the heat load from the infrared detectors. Consequently, the rather unsatisfactory options are either to include two visible spectrographs for land and sea, with spatial resolutions of 0.5 and 1.0 km, or to degrade the spatial resolution of all visible imagery to 1.0 km.

3.5 Infrared Imager.

The specifications for the infrared imager are listed in Table 8. The proposed design uses dichroic beam splitters to separate the long, medium and shortwave infrared components, as indicated in Figure 10. A sensitivity analysis for the imager, based upon manufacturers' guaranteed detectivities, is presented in Appendix 3 to show that the specifications can be achieved.

For a telescope with a clear circular aperture whose diameter is D, the angular radius of the Airy disc produced by a point source at infinity is

$$1.22\ \lambda/D \quad .$$

According to Rayleigh's classical argument, 84% of the available energy falls within the Airy disc. For a satellite telescope, the source is extended and fills the entire field of view defined by the field stop. In this case, Goldberg and McCulloch (1968) suggested that a practical definition of resolution is the size of the region which contains 84% of the energy from the field of view. For the ISAS telescope, with a 2.0 km field of view and 25% obscuration, the effective resolution turns out to be 3.0 km at 10 μm, so the telescope is diffraction limited.

TABLE 8. Infrared imager performance.

Wavelength range μm	Spatial resolution km	Number of pixels	NEΔT (spec) K	NEΔT (expected) K	Scene temp K
2.05 - 2.35	2	16	0.10%*	0.028%*	300
3.80 - 4.00	2	16	0.10	0.039	300
6.50 - 7.00	2	16	0.50	0.295	230
10.20 - 11.20	2	16	0.10	0.022	300
11.50 - 12.50	2	16	0.10	0.086	300

* The figures quoted for the 2.2 μm channel are the noise equivalent differential albedo, NE$\Delta\rho$.

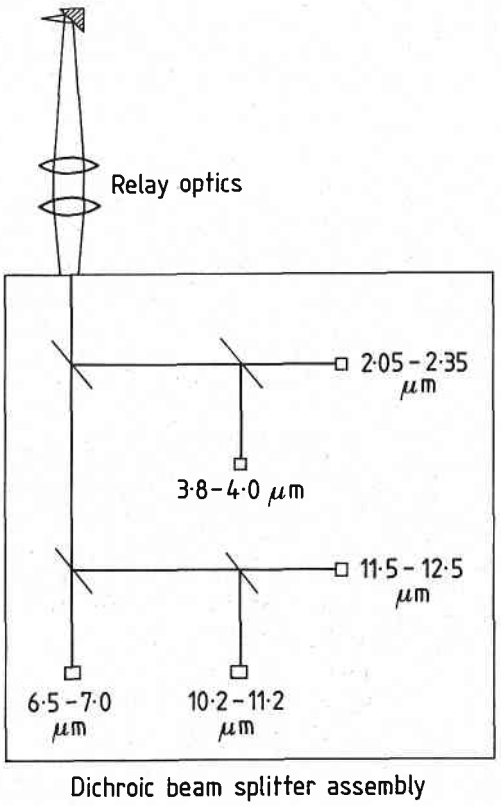

Figure 10: Infrared imager schematic.

3.6 Infrared Sounder.

There are three options for the infrared sounder:

(i) a filter wheel instrument, such as the HIRS instrument, currently deployed on the NOAA satellites and soon to be deployed on GOES NEXT;

(ii) a Michelson interferometer, such as the HIS instrument, proposed by Smith et al. (1979) at the University of Wisconsin;

(iii) an infrared spectrometer using gratings as the dispersive elements and two dimensional detector arrays.

The filter wheel radiometer offers proven technology. Some might argue that it is outdated technology, since the original design for the HIRS instrument is nearly 20 years old. However, its advantages are that:

- few detectors are needed;
- the signal to noise ratio can be improved with cold filters, to reduce longwave background thermal flux, and with aplanats, to reduce the system focal ratio to better than f/1, so that smaller detectors can be used.

Its principal disadvantages are that:

- sequential sampling of the several channels wastes dwell time;
- the channels are fixed at launch.

The sounder on GOES NEXT will be a minor modification of the HIRS instrument. Since the telescope proposed for ISAS has twice the diameter of that for GOES NEXT, but other factors such as sounder footprint and scan time are approximately equal, it is clear that a HIRS instrument could be appended as the infrared sounder package for ISAS.

According to Smith et al. (1979), an interferometer offers a significant improvement in passive sounding capability. A prototype for HIS has been constructed for the University of Wisconsin by Bomem and the Santa Barbara Research Centre, and trials from a U2 aeroplane were conducted recently. The reported results are encouraging (Smith et al. (1986)). The advantages of an interferometer are that:

- few detectors are needed;
- the resolution and the spectral region can be placed under ground control.

Its principal disadvantages are that:

- the instrument requires a long dwell time to achieve high spectral resolution, because the displacement of the interferometer mirror may need to be as large as 10 cm;
- the instrument involves moving mirrors and alignment of the system must be achieved dynamically with an auxiliary interferometer system.

The HIS instrument could not be incorporated into the present proposal without significant modifications to its optics. Firstly, HIS includes its own telescope. Secondly, a counter-rotating mirror would be needed to compensate for the motion of the scan mirror in order to achieve adequate dwell times. However, the concept of using an interferometer is attractive, especially if the interferometer aims for lower spectral resolution (such as 10 cm^{-1}) so that smaller mirror displacements (0.1 cm) and shorter dwell times would suffice.

The third option, which uses a grating spectrometer, is technically the simplest. To achieve high grating efficiencies, the beam must be split into short, medium and long wavelength components with dichroic beam splitters and a separate grating used for each spectral region. The analysis of Appendix 5 shows that efficiencies in excess of 75% are then possible and that the required resolution can be achieved with 25 mm optics, with a configuration such as that shown in Figure 11.

The advantages of the grating spectrograph are:

- no moving parts;
- all channels are sampled simultaneously.

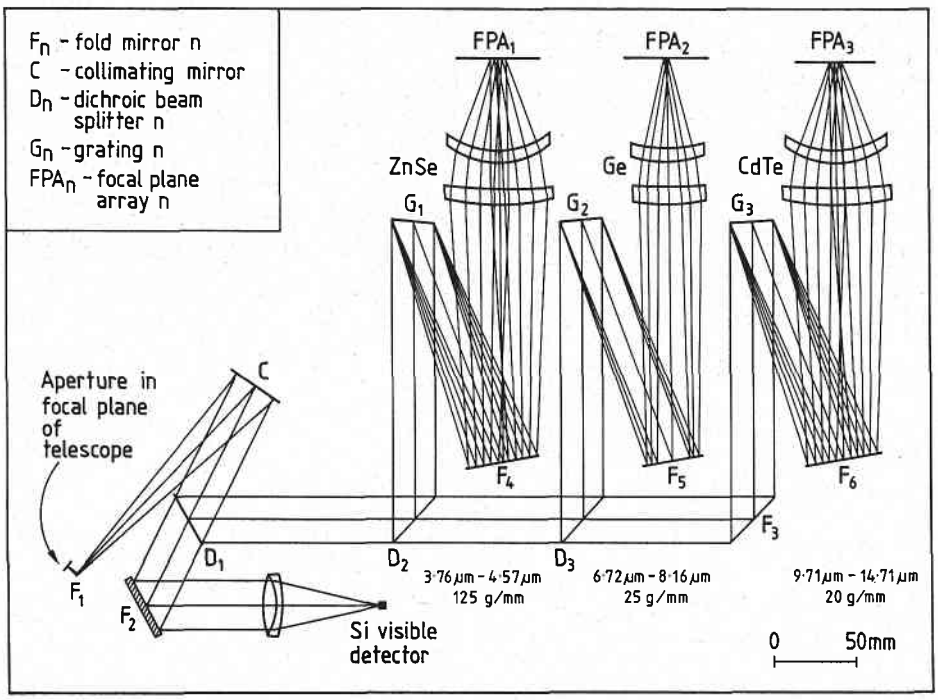

Figure 11: Grating spectrometer schematic.

Its disadvantages are:

- the detectors must be placed in a focal plane rather than a pupil plane;
- infrared detector arrays are needed;
- the channels are fixed at launch.

Detector arrays pose a problem because the heat they generate is difficult to dissipate. Infrared detectors require cooling to reduce thermal background noise. For example, in the AVHRR and GOES NEXT instruments, the detector temperature is 100 - 105 K, whereas GOES NOW maintains its detectors at 80 - 85 K. Detectors are used in the photovoltaic mode for wavelengths up to about 8 μm, in which case the joule heating in the detectors is minimal, but at longer wavelengths, where mercury-cadmium-telluride (HgCdTe) detectors must be operated in the photoconductive mode, the opposite is true. Since the power dissipated by the detectors must be radiated to space, the size of the radiative cooler can become prohibitive if the detector dissipation is large.

When detectors are placed in the focal plane, it is possible for hot spots on the ground to coincide with hot spots on the detectors and lead to unrepresentative signals. This problem is only significant for the 15 μm CO_2 bands, where difficulties in the fabrication of HgCdTe detectors can lead to significant variations in the composition of the alloy across the detector pixels. At present, the only way in which these problems can be overcome is to keep the size of the detectors as small as possible, a fact which additionally helps in reducing noise. Details are given in Appendix 6.

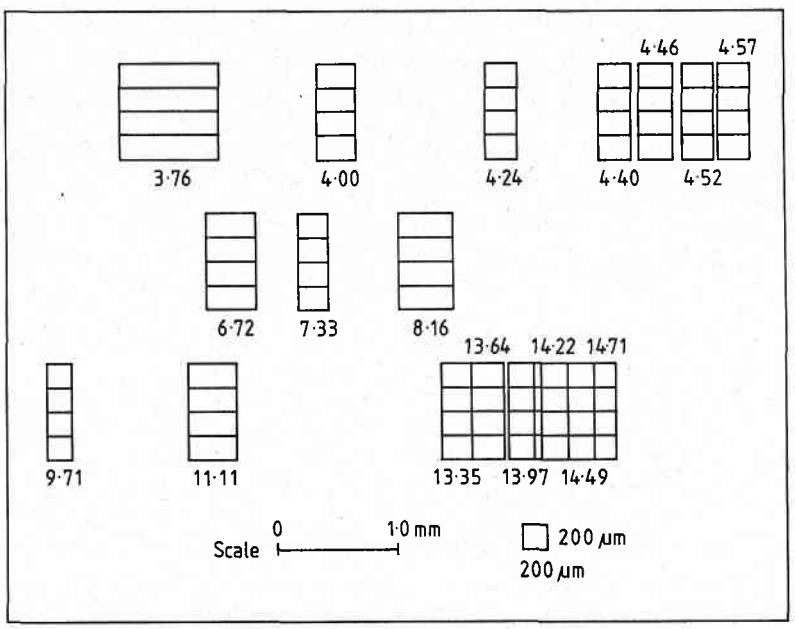

Figure 12: Focal plane array for the infrared sounder.

The detailed sensitivity analysis for a grating spectrometer is given in Appendix 5, but the principal results are summarised in Table 9, where the predicted noise equivalent differential radiances are compared with those for the improved HIRS/2I instrument, which will be flown on the next series of TIROS satellites. The analysis assumes that a focal plane array has been fabricated so that the detector elements correspond to the standard HIRS channels, as shown in Figure 12. It is clear from Table 9 that the HIRS specifications can be exceeded from geosynchronous orbit.

TABLE 9. Sounder performance.

HIRS channel #	λ	$\Delta\lambda$	NEΔN	
			HIRS/2I	ISAS
	μm	μm	mW m^{-2} sr^{-1}	$(cm^{-1})^{-1}$
2	14.71	0.216	0.50	0.275
3	14.49	0.252	0.53	0.248
4	14.22	0.324	0.29	0.211
5	13.97	0.312	0.20	0.201
6	13.64	0.298	0.24	0.202
7	13.35	0.285	0.20	0.198
8	11.11	0.432	0.10	0.056
9	9.71	0.236	0.15	0.058
10	8.16	0.400	0.16	0.035
11	7.33	0.215	0.20	0.038
12	6.72	0.361	0.19	0.025
13	4.57	0.048	0.006	0.0015
14	4.52	0.047	0.003	0.0015
15	4.46	0.046	0.004	0.0014
16	4.40	0.045	0.002	0.0014
17	4.24	0.041	0.002	0.0014
18	4.00	0.055	0.002	0.0010
19	3.76	0.141	0.001	0.0006

3.7 Radiative Cooler.

The radiative cooler will be a three stage device with:

(1) an inner patch at 100 K, upon which the detectors will be mounted;

(2) a radiator at 150 K;

(3) a sunshield at 240 K.

Of the several options presented for the infrared sounder, the most difficult to cool is the grating spectrometer, because it has the most detectors, so this case is considered in the design of the cooler presented in Appendix 7.

Figure 13 shows the diameter of the patch as a function of the detector power dissipation, with all other factors assumed constant. Realistic estimates of the detector dissipation are listed in Table 10.

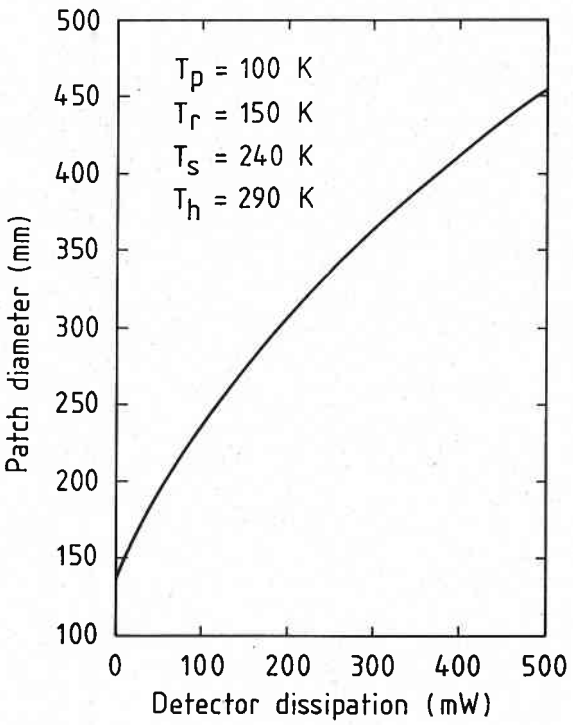

Figure 13: Patch diameter as a function of detector dissipation.

TABLE 10. Infrared detector power dissipation.

Instrument	material	channels	pixels	detectors	size μm	power/ element mW	total power mW
IR imager	PV InSb	3	16	48	50	0.25	12
	PC HgCdTe	2	16	32	50	0.25	8
IR sounder	PV InSb	7	4	28	250	1.25	35
	PV HgCdTe	3	4	12	250	1.25	15
	PC HgCdTe	8	4	32	250	7.50	240
							310

Thus, the total detector power to be dissipated is likely to be 310 mW, in which case the patch diameter would be 370 mm. This is large by current instrument standards, but it is not unreasonable given the size of all other components of ISAS.

For completeness the expected dissipation of the visible detectors is listed in Table 11.

TABLE 11. Visible detector power dissipation.

Instrument	material	channels	pixels	detectors	size μm	power/ array mW	total power mW
Vis imager	Si	20	64	1280	50	60	60
Vis sounder	S	1	4	4	200	neglible	

3.8 Size, Weight and Power.

On the basis of the GOES NEXT instruments, it is possible to estimate the size, weight and power requirements of ISAS. Figure 14 is a suggested mechanical layout with dimensions 2000 x 860 x 860 mm and estimated weight 365 kg. Breakdowns of the weight, based on flight proven modules and direct extension of known designs, and comparisons with other instruments are presented in Tables 12 and 13.

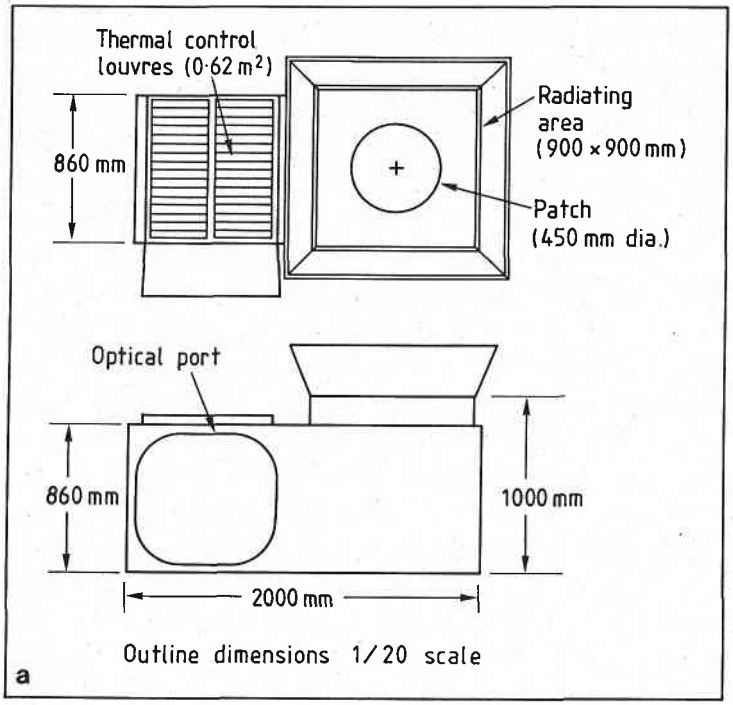

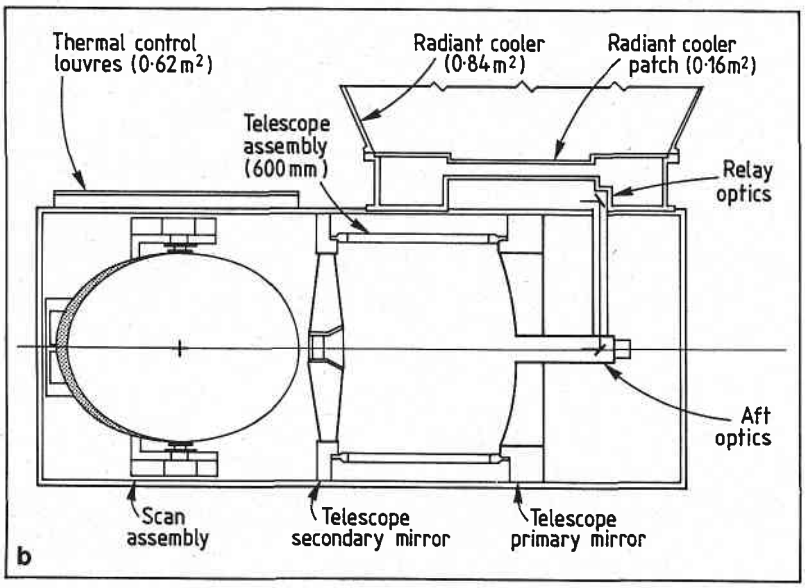

Figure 14: (a) Outline dimensions, (b) Instrument layout.

TABLE 12. Size and weight estimates.

Module	Sub assembly	Weight (kg)
Sensor module	Structure assembly	168
	Aft optics	3
	Relay optics assembly	7
	Telescope assembly	42
	Scanner assembly	47
	Radiant cooler assembly	20
Electronics module		61
Power supply module		17
Estimated total instrument weight		365
Uncertainty (+20%)		73
Total instrument weight range		365 - 438

TABLE 13. Weight and power comparisons.

INSTRUMENT	DIAM	SIZE		WEIGHT		
		Sensor	Electronics	Sensor	Electronics	Total
	mm	mm	mm	kg	kg	kg
INSAT VHRR	200	275x288x606	305x250x353	28	15	43
AVHRR/2	200	283x360x755		29		29
HIRS	200	300x315x640		33		33
GOES/imager	300	450x470x1025	125x325x375	72	39	111
GOES/sounder	300	450x470x1025	125x325x375	80	37	117
ISAS	600	860x860x2000		287	78	365

The likely power breakdown is shown in block form in Figure 15 and compared with the breakdown for GOES NEXT in the Table 14.

Note that the power for the analog data channels and detectors is reckoned at 1.0W per channel plus the dissipation in the detectors. The power profile for ISAS is expected to be very similar to that for GOES NEXT, shown in the Table 15.

TABLE 14. Power comparisons.

Function		GOES NEXT IMAGER scan W	GOES NEXT IMAGER turn W	GOES NEXT SOUNDER dwell W	GOES NEXT SOUNDER step W	ISAS scan W	ISAS turn W
Digital processing & data out		1.00	1.00	1.00	1.00	1.00	
Clock timing & control		0.25	0.25	1.50	1.50	1.50	
Analog data channels & detectors		15.05	15.05	15.44	15.44	44.37	
Servo electronics		10.00	10.00	10.00	10.00	10.00	
Command & telemetry (standby)		3.00	3.00	3.00	3.00	3.00	
Total		29.30	29.30	30.94	30.94	59.87	
Regulator input	(85% eff.)	34.47	34.47	36.40	36.40	70.44	
Filter wheel drive				6.90			
Turnaround or step			40.00		30.00		40.00
Converter output		34.47	74.47	43.30	66.40	70.44	110.44
Converter input	(90% eff.)	38.30		48.11		78.26	
	(94% eff.)		79.22		70.64		117.48
Switching regulator	(85% eff.)	45.06		56.60		92.07	
	(90% eff.)		88.03		78.49		130.54

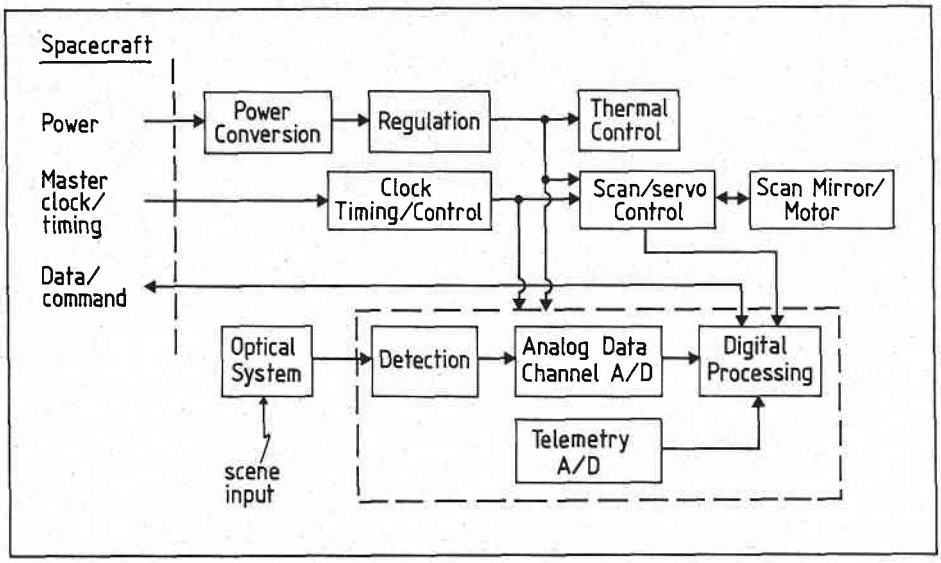

Figure 15: Power breakdown.

TABLE 15. Power profile for GOES NEXT.

Function	GOES NEXT IMAGER W	GOES NEXT SOUNDER W
Thermal control peak	46.4	46.4
Thermal control average	29.7	29.7
Decontamination peak	73.0	73.0
Average during scan/sounding	43.8	57.4
Daily average	73.5	87.1
Daily peak	131.6	131.0
Standby	4.6	4.6
Outgas plus standby	77.6	77.6

3.9 Data Rate.

The data rate is dominated by the output from the visible imager, as shown in Table 16. Figure 16 is a rough schematic for the signal processing system.

TABLE 16. Data rate for ISAS.

Instrument	pixels	channels	bits	dwell msec	data rate Mbps
Visible imager	64	20	12	1.116	13.763
Infrared imager	32	5	12	2.232	0.860
Infrared sounder	4	19	12	8.923	0.009
					14.632

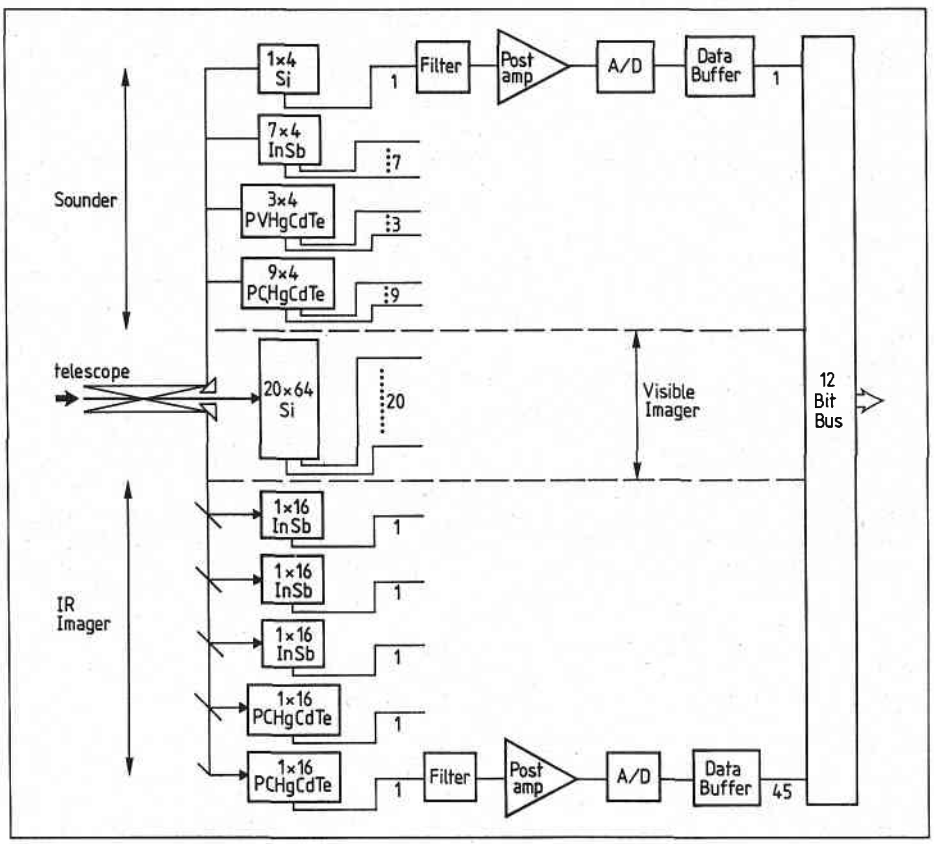

Figure 16: Signal processing schematic.

4.0 REFERENCES.

Goldberg, I.L., and McCulloch, A.W., Annular aperture diffracted energy distribution for an extended source, Goddard Space Flight Center Preprint X-622-68-132, April 1968.

Joint CSIRO/Bureau of Meteorology proposal for a remote sensing package (imager and sounder) to be flown on a geostationary satellite over the Australian region, April 1986, CSIRO Division of Atmospheric Research, Private Bag # 1, Mordialloc, Victoria 3195, Australia.

Smith, W.L., Howell, H.B., and Woolf, H.M., The use of interferometric radiance measurements for sounding the atmosphere, J. Atmos. Sci, 36 (1979) 566 - 575.

Smith, W.L., Revercomb, H.E., Howell, H.B., Woolf, H.M., and LaPorte, D.D., The high resolution interferometer sounder (HIS), CIMSS View, Vol II, No. 3 (1986) 1 - 5.

5.0 ACKNOWLEDGEMENTS.

The basis of the design contained in this report was established in discussions with Ian Wilson and Clyde Mitchell of CSIRO Division of Materials Science and Technology, and subsequently developed during a two week visit to the Aerospace/Optical Division of ITT at Fort Wayne, Indiana, in January 1987. During this time we worked in close collaboration with a team of ITT personnel led by Ron Koczor, and we benefitted greatly from their expertise and experience in satellite instrument design and manufacture. Particular thanks are due to the following: Brian Cohn (optical design), Truxton Fulton (detectors), Roy Galvin (radiative cooler), Rick Mescher (mechanical design), Eric Scheithauer (electronics), Gary Stephenson (sensitivity analysis) and Dave Yeager. Valuable contributions were also made by Jim Crawford, Dick Harber, Gerry Sonnek, Jean Vasicek and Jack Wilcox. Larry Owens conducted an interesting and informative tour of the AVHRR testing facility. We thank Dom Juarez and Bill Knorr for their hospitality and for providing the opportunity for us to visit the Division.

Funding for the trip was made available through the CSIRO Office of Space Science and Applications (COSSA).

6.0 APPENDICES.

1. Optics of the visible spectrometer.
2. Visible spectrometer sensitivity analysis.
3. Infrared imager sensitivity analysis.
4. Grating spectrometer design.
5. Grating spectrometer sensitivity analysis.
6. Impact of non-uniformity in HgCdTe detectors.
7. Radiant cooler design.

NOTATION.

The following notations will prevail throughout the appendices.

d_o	:	diameter of the telescope optics	(600 mm)
A_o	:	area of the telescope optics	
τ_o	:	transmission of the optical system, including obscuration by the telescope	
Ω	:	solid angle subtended by the footprint at the satellite	
P_d	:	power incident upon the detector	
A_d	:	area of the detector	
I_d	:	detector current	
Δf	:	amplifier bandpass	
ρ	:	albedo of target	
F_ν	:	solar flux density at frequency ν	
F_λ	:	solar flux density at wavelength λ	
B_ν	:	black body radiance at frequency ν	
B_λ	:	black body radiance at wavelength λ	

APPENDIX 1. Optics of the visible imager.

Figure 17 presents a first pass design of the visible imaging spectrometer. The choice of material for the prism (SF5 glass) is not optimal, because the dispersion is a strongly nonlinear function of wavelength, as shown in Figure 18. However, this design does indicate that:

(1) the spectrometer requires only small diameter optics;

(2) the prism angle need only be small (approximately 6°) to achieve adequate dispersion if a highly dispersive glass such as SF5 is used.

In practice cemented prisms of different materials would be used. With a 10:1 ratio for BK7:SF11, the variation in dispersion from 400 to 900 nm is reduced to a factor of five, as shown in Figure 9. This dispersion is well represented by a curve with the form

$$\frac{dn}{d\lambda} = (b^2\lambda^2 - a^2)^{-1} \quad ,$$

with

$$a = 58.699 \quad , \qquad b = 0.34133 \qquad \text{for wavelength in nm} \quad .$$

Distance x in the focal plane of the spectrometer is approximately related to dispersion by

$$dx = f\alpha \frac{dn}{d\lambda} d\lambda \quad ,$$

where f is the focal length of the refocusing lens and α is the angle of the prism. The relation between x and λ which follows is

$$\lambda = a/(b \tanh \mu) \quad ,$$

where

$$\mu = ab\,(c - x/(f\alpha)) \quad .$$

The constant c is fixed so that the beginning of the spectrum λ_0 falls at x = 0, whereas α is fixed so that the end of the spectrum λ_1 falls at $m\delta x$, where m is the number of detector pixels and δx is their length. Thus,

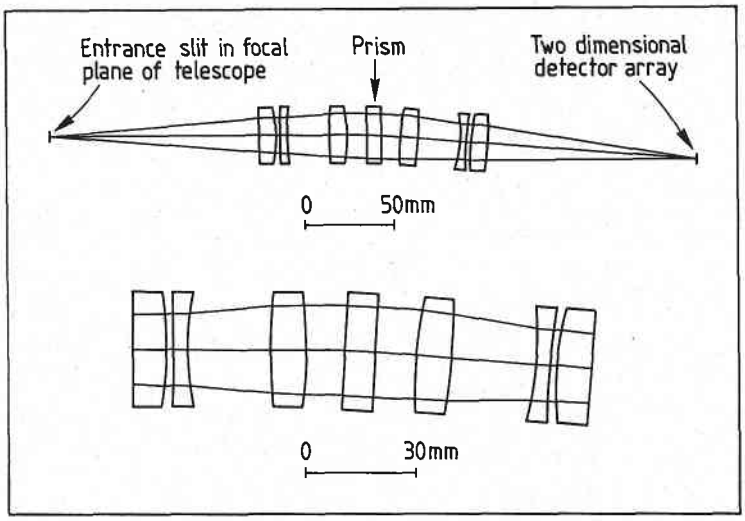

Figure 17: Visible spectrometer design.

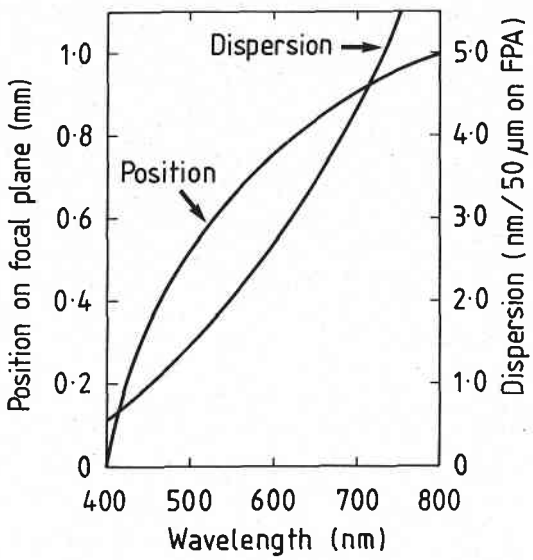

Figure 18: Dispersion of the visible spectrometer.

APPENDIX 2. Visible spectrometer sensitivity analysis.

The dominant noise sources are:

(1) Johnson noise,

$$i_j^2 = 4kT \Delta f/R \ ;$$

(2) shot noise,

$$i_s^2 = 2eI_d \Delta f \ ;$$

(3) amplifier noise, i_a, which consists of two terms, the first arising from a voltage source v_a developed across R, and the second arising from an equivalent current source within the amplifier.

The symbols used here are defined as follows:

k is Boltzmann's constant, 1.381×10^{-23} J K^{-1};

e is the electronic charge, 1.602×10^{-19} C;

T is the detector temperature;

Δf is the noise bandwidth;

R is the parallel combination of the detector dynamic resistance and the feedback resistance.

The signal current I_d is related to the power P_d incident on the detector via

$$I_d = R_d P_d \ ,$$

where R_d is the detector responsivity. Over the wavelength range from 400 to 900 nm, the responsivity of Si is well represented by

$$R_d = 0.6 \ (\lambda - 330)/(935 - 330) \ AW^{-1} \ .$$

The power onto the detector is

$$P_d = \frac{F_\lambda \Delta\lambda \rho}{\pi} \ \Omega \ A_o \ \tau_o \ ,$$

where the symbols have been defined previously.

The signal to noise ratio is

$$SNR = I_d/i_n \ ,$$

where

$$i_n = (i_j^2 + i_s^2 + i_a^2 + (v_a/R)^2)^{\frac{1}{2}} \ .$$

TABLE 17. Signal to noise ratio for the visible imager.

#	λ nm	Δλ nm	0.5 km resolution albedo 100%	0.5 km resolution albedo 10%	0.5 km resolution albedo 1%	1.0 km resolution albedo 100%	1.0 km resolution albedo 10%	1.0 km resolution albedo 1%
1	405.5	10.9	135.1	15.1	1.5	420.9	57.9	6.1
2	416.7	11.6	163.5	18.6	1.9	492.3	71.1	7.5
3	428.7	12.3	177.3	20.4	2.1	525.7	77.6	8.3
4	441.4	13.1	243.4	29.5	3.0	678.0	109.7	12.0
5	455.0	14.0	296.6	37.4	3.9	793.6	136.7	15.3
6	469.5	15.0	334.4	43.3	4.5	873.1	156.5	17.7
7	485.1	16.1	371.6	49.4	5.1	949.6	176.4	20.3
8	501.8	17.3	418.4	57.5	6.0	1044.2	202.0	23.7
9	519.8	18.7	459.1	64.9	6.8	1125.3	224.8	26.9
10	539.3	20.2	511.0	74.7	7.9	1227.4	254.5	31.1
11	560.3	21.9	560.2	84.5	9.0	1323.1	283.1	35.3
12	583.1	23.8	635.8	100.4	10.9	1469.3	328.1	42.3
13	608.0	26.0	692.7	113.0	12.4	1578.6	362.6	47.9
14	635.3	28.5	756.0	127.7	14.1	1699.8	401.6	54.6
15	665.2	31.3	821.3	143.5	16.1	1824.8	442.3	61.8
16	698.2	34.6	888.4	160.4	18.2	1953.0	484.6	69.6
17	734.7	38.5	958.4	178.7	20.6	2086.9	529.1	78.2
18	775.4	43.0	1025.9	197.0	23.0	2216.0	572.3	87.0
19	821.1	48.3	1068.0	208.6	24.6	2296.6	599.3	92.6
20	872.6	54.7	1164.4	236.0	28.4	2481.6	661.6	106.0

Table 17 presents the signal to noise ratio for 0.5/1.0 km resolution (14/28 μrad field of view) and surface albedos of 100%, 10% and 1%. The values of the other parameters are as follows:

$$T = 300\ K\ ;$$

$$\Delta f = 560\ Hz\ ;$$

$$R = 1 \times 10^{9}\ \Omega\ ;$$

$$\tau_o = 0.6\ ;$$

$$i_a = 1 \times 10^{-15}\ AHz^{-\frac{1}{2}}\ ;$$

$$v_a = 1 \times 10^{-9}\ VHz^{-\frac{1}{2}}\ .$$

The sensitivities of the CZCS channels are specified at representative values of the radiance expected at the satellite, rather than in terms of a surface albedo. In order to facilitate comparison of CZCS and ISAS, Table 18 presents the signal to noise ratios for the two instruments calculated with the albedo which produces the radiance assumed in the CZCS specifications.

TABLE 18. Comparison of ISAS and CZCS signal to noise ratios.

		ISAS				CZCS		
albedo	#	λ	Δλ	SNR 0.5 km	SNR 1.0 km	λ	Δλ	SNR 0.8 km
9.4%	4	441.4	13.1	27.8	103.7	443	20	>150
6.0%	9	519.8	18.7	39.8	144.8	520	20	>140
5.2%	11	560.3	21.9	45.5	163.6	550	20	>125
2.9	15	665.2	31.3	45.5	163.5	670	20	>100
27.5%	18	775.4	43.0	439.0	1085.4	750	20	>100

APPENDIX 3. Infrared imager sensitivity analysis.

The signal to noise ratio for an infrared detector is

$$SNR = P_d D^* / \sqrt{A_d \Delta f} ,$$

where D* is the specific detectivity of the detector, and P_d is the power incident upon the detector.

$$P_d = \tau_o A_o \Omega B_\nu \Delta\nu .$$

The noise bandwidth is assumed to be related to the dwell time t_d and scan efficiency η by

$$\Delta f = 1/(2\eta t_d) .$$

The noise equivalent differential radiance, NEΔN, and noise equivalent differential temperature, NEΔT, are defined by

$$NE\Delta N^{-1} = \frac{\partial}{\partial B_\nu} (SNR) ,$$

$$NE\Delta T^{-1} = \frac{\partial}{\partial T} (SNR) .$$

The values used for the specific detectivity in the sensitivity calculations below are the minimum specifications guaranteed by the manufacturer, with due allowance for 1/f noise and reduced angular aperture of the final optics at the detector.

The first correction arises because the manufacturer's specifications are quoted at a frequency, f_0, which lies below the knee frequency, f_k, where the 1/f noise merges into the generation-recombination noise of the detector. If the frequencies at which the bandpass falls to half power are f_1 and f_2, then it is not difficult to show that the D* should be derated by

$$\alpha = \left[\left(\frac{f_k}{f_k + f_0} \right) \left(\frac{f_o}{f_k} + \frac{f_o}{f_2 - f_1} \log \frac{f_2}{f_1} \right) \right]^{\frac{1}{2}} .$$

For the infrared imager,

$$f_0 = 100 \text{ Hz},$$

$$f_k = 300 \text{ Hz},$$

$$f_1 = 5 \text{ Hz},$$

$$f_2 = 285 \text{ Hz},$$

so

$$\alpha = 1.155 \quad .$$

The second correction allows for the reduction of the aperture to the detector by a cold stop, whose purpose is to reduce the background thermal flux which reaches the detector. For a point detector and optics with final focal ratio $f^{\#}$, the field of view theoretically could be limited to a cone with half angle of $1/\sin(0.5/f^{\#})$. It will be assumed that the system focal ratio can be reduced to f/1.5, in which case the cone half angle is approximately 20°, and the detector size is 50 μm.

The calculation of the throughput for the imager is summarised in Table 19. A nominal value of 30% has been assumed for the throughput in the sensitivity calculations. The performance predicted for the infrared imager is summarised in Table 20.

TABLE 19. Throughput of the infrared imager.

Channel (μm)	2.20	3.90	6.75	10.70	12.00
Scan mirror	0.97	0.97	0.97	0.97	0.97
Obscuration	0.94	0.94	0.94	0.94	0.94
Telescope	0.97^2	0.97^2	0.97^2	0.97^2	0.97^2
Relay optics	0.95^2	0.95^2	0.95^2	0.95^2	0.95^2
Dichroics (trans)	0.87	1.00	0.87^2	0.87	0.87^2
Dichroics (refl)	0.97	0.97^2	1.00	0.97^2	0.97
Refocus lens	0.95	0.95	0.95	0.95	0.95
Housing window	0.85	0.85	0.85	0.85	0.85
Radiator window	0.85	0.85	0.85	0.85	0.85
Filter bandpass	0.77	0.77	0.77	0.77	0.77
Aplanat	0.95	0.95	0.95	0.95	0.95
	0.33	0.37	0.29	0.32	0.29

TABLE 20. Infrared imager performance.

	Units	Channel 1	2	3	4	5
λ_{max}	μm	2.35	4.025	7.00	11.20	12.50
λ_{min}	μm	2.05	3.775	6.50	10.20	11.50
$\Delta\lambda$	μm	0.30	0.25	0.50	1.00	1.00
$\Delta\nu$	cm^{-1}	619.80	164.40	109.70	87.34	69.44
Δf	Hz	280.00	280.00	280.00	280.00	280.00
τ_o		0.30	0.30	0.30	0.30	0.30
1/sin 20°		2.924	2.924	2.924	2.924	2.924
α		1.000	1.000	1.155	1.155	1.155
D* (spec)	$cmHz^{\frac{1}{2}}W^{-1}$	5.0×10^{10}	4.4×10^{11}	2.6×10^{10}	3.8×10^{10}	1.2×10^{10}
D*	$cmHz^{\frac{1}{2}}W^{-1}$	1.5×10^{11}	1.3×10^{12}	6.6×10^{10}	9.6×10^{10}	3.0×10^{10}
Size	μm	50	50	50	50	50
Temp	K		300	230	300	300
$\partial B_\nu/\partial T$	$Wm^{-2}sr^{-1}(cm^{-1})^{-1}K^{-1}$		3.755×10^{-5}	1.474×10^{-4}	1.680×10^{-3}	1.751×10^{-3}
$\partial B_\nu/\partial T\ \Delta\nu$	$Wm^{-2}sr^{-1}K^{-1}$		6.172×10^{-3}	1.617×10^{-2}	1.467×10^{-1}	1.216×10^{-1}
NEΔT	K		0.039	0.295	0.022	0.086
F_ν	$Wm^{-2}(cm^{-1})^{-1}$	3.824×10^{-2}				
$F_\nu\Delta\nu$	Wm^{-2}	$2.370\times10^{+1}$				
NE$\Delta\rho$		0.028%				

APPENDIX 4. Grating spectrometer design.

A grating spectrometer intended to span the wavelength range of the sounder (3.6 μm - 15 μm) requires three gratings in order to achieve reasonable efficiency and to prevent overlapping of orders. Consequently, in the design shown in Figure 11, the visible channel and the short, medium and long wavelength components are separated with dichroic beam splitters prior to spectral analysis.

The angular size of the detector at the last lens of the spectrometer is

$$\Delta\phi = \frac{d_o}{d_s} \Delta\theta ,$$

where d_o and d_s are the diameters of the telescope and spectrometer optics, and where $\Delta\theta$ is the angular size of the field of view. Thus, the dispersion required of the grating is

$$\frac{\Delta\phi}{\Delta\lambda} = \frac{d_o}{d_s} \frac{\Delta\theta}{\Delta\lambda}$$

if the detector is intended to span $\Delta\lambda$. From the dispersion can be calculated the size and line spacing of the grating, and finally the blaze angle can be selected to optimise the throughput over the wavelength range. Such calculations led to the gratings suggested in Table 21. The linear dispersion quoted in the last column of Table 21 assumes a focal length of 45mm for the refocusing lens.

The final focal ratio shown in Figure 11 is f/3. However, the aberrations of that design are so small that it has been assumed throughout the sensitivity analysis that the focal ratio can be reduced to f/1.5.

TABLE 21. Grating specifications.

#	λ_{min} μm	λ_{max} μm	λ_{blaze} μm	θ_{blaze}	line gap μm	eff	$\Delta\phi/\Delta\lambda$ μm^{-1}	$\Delta x/\Delta\lambda$ $mm\ \mu m^{-1}$
1	3.60	5.00	4.00	14.5°	8	>75%	0.129	5.810
2	6.60	8.16	7.50	5.4°	40	>75%	0.025	1.130
3	9.71	14.71	12.25	7.0°	50	>75%	0.020	0.909

The sounder throughput is calculated in Table 22. The throughput used in the sensitivity calculations is 30% for short, medium and long wavelengths.

TABLE 22. Sounder throughput.

	Shortwave	Mediumwave	Longwave
Scan mirror	0.97	0.97	0.97
Obscuration	0.94	0.94	0.94
Telescope	0.97^2	0.97^2	0.97^2
Fold mirrors	0.97^4	0.97^4	0.97^5
Dichroics (tran)	1.00	0.87	0.87^2
Dichroics (refl)	0.97^2	0.97^2	0.97
Grating	0.75	0.75	0.75
Lens system	0.95^2	0.95^2	0.95^2
Housing window	0.85	0.85	0.85
Radiator window	0.85	0.85	0.85
	0.36	0.31	0.27

APPENDIX 5 Grating spectrometer sensitivity analysis.

The calculation of the signal to noise ratio and noise equivalent differential radiances for the sounder is similar to the calculation for the infrared imager. The principal differences are as follows.

(1) The noise bandwidth is Δf = 35 Hz, with

$$f_1 = 0.5 \text{ Hz},$$

$$f_2 = 35.5 \text{ Hz}.$$

The specification frequency f_0 and knee frequency f_k have the previous values,

$$f_0 = 100 \text{ Hz},$$

$$f_k = 300 \text{ Hz}.$$

Thus, the derating factor for the detector D* is

$$\alpha = 3.063.$$

(2) The focal ratio of the refocusing optics is f/1.5, so the field of view for a point detector could be limited with a cold stop to a cone with half angle 20°. In practice, the cone angle would need to be larger, typically 25°, because the detectors are extended arrays. Thus, the detector D* (quoted for 90° by the manufacturer) can be improved by a factor of

$$1/\sin 25° = 2.366 .$$

Figure 19 shows a scale diagram of the final optical stage and indicates the arrangement of the cold ports.

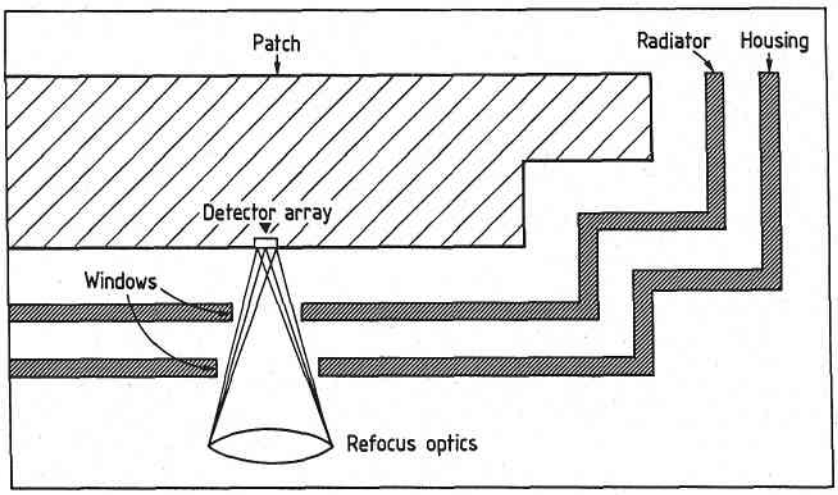

Figure 19: Optical ports into the cooler patch.

The results of these calculations are summarised in Table 23. It is assumed that a focal plane array has been fabricated so that the detector elements correspond to the standard HIRS channels, as shown in Figure 12.

TABLE 23. Detectivities for the sounder.

	Shortwave	Mediumwave	Longwave
α	1.000	3.063	3.063
1/sin 25°	2.366	2.366	2.366
D* (spec)	4.1×10^{11}	2.6×10^{10}	1.3×10^{10}
D* (net)	9.7×10^{11}	2.0×10^{10}	1.0×10^{10}

The angular size of the detector at the last lens of the spectrometer is

$$\Delta\phi = \frac{d_o}{d_s} \Delta\theta \quad ,$$

so its physical size is

$$\Delta a = f \Delta\phi \quad ,$$

where f is the focal length of the refocusing optics. This reduces to

$$\Delta a = f^{\#} d_o \Delta\theta \quad ,$$

where $f^{\#}$ is the final focal ratio, because the diameters of the collimating and refocusing optics are equal. The height of each detector pixel is determined by the angular spread of the field of view,

$$\Delta h_d = f^{\#} d_o \Delta\theta_{fov} \quad ,$$

whereas the width is determined by the dispersion of the grating,

$$\Delta w_d = f^{\#} d_o \left(\frac{\Delta\phi}{\Delta\lambda} \Delta\lambda\right) \quad .$$

The spectrometer is assumed to have a final optical speed of f/1.5, so the height of each pixel in the detector array is 200 micrometres. The widths corresponding to the different spectral channels and the noise equivalent differential radiances are listed in Table 24.

TABLE 24. Sounder performance.

#	ν	$\Delta\nu$	λ	$\Delta\lambda$	Δw_d	$\sqrt{A_d}$	$NE\Delta N$*	$NE\Delta T$	Scene temp
	cm^{-1}	cm^{-1}	μm	μm	μm	μm		K	K
1	680	10	14.71	0.216	196	198	0.275	0.201	265
2	690	12	14.49	0.252	229	214	0.248	0.223	240
3	703	16	14.22	0.324	295	243	0.211	0.174	250
4	716	16	13.97	0.312	284	238	0.201	0.147	265
5	733	16	13.64	0.298	271	233	0.202	0.132	280
6	749	16	13.35	0.285	259	228	0.198	0.121	290
7	900	35	11.11	0.432	393	280	0.056	0.026	330
8	1030	25	9.71	0.236	215	207	0.058	0.053	270
9	1225	60	8.16	0.400	452	301	0.035	0.033	290
10	1365	40	7.33	0.215	243	221	0.038	0.061	275
11	1488	80	6.72	0.361	408	286	0.025	0.076	260
12	2190	23	4.57	0.048	279	236	0.0015	0.012	300
13	2210	23	4.52	0.047	273	234	0.0015	0.018	290
14	2240	23	4.46	0.046	267	231	0.0014	0.025	280
15	2270	23	4.41	0.045	261	229	0.0014	0.059	260
16	2360	23	4.24	0.041	238	218	0.0014	0.038	280
17	2515	35	3.98	0.055	320	253	0.0010	0.007	340
18	2660	100	3.76	0.141	819	405	0.0006	0.006	340

* Note that the units for $NE\Delta N$ are $mWm^{-2}sr^{-1}(cm^{-1})^{-1}$.

APPENDIX 6. Impact of non-uniformity in HgCdTe detectors.

The purpose of this appendix is to investigate the effects of 'hot spots' in HgCdTe detectors. The specific detectivity of the hot spots is assumed to be enhanced from D* to D*(1 + d), and the fraction of the total area A_d occupied by hot spots is assumed to be x. The worst case to be considered occurs when hot spots on the ground, where the temperature is T + ΔT, are imaged onto the hot spots of the detector. The calculations find the value of d which leads to a difference of one between the signal to noise ratios of detectors with and without hot spots. When this is the case, the detector hot spots produce effects larger than the noise and hence degrade the system performance.

Let SNR_{1-x} and SNR_x denote the contributions to the signal to noise ratio from the parts of the scene with temperatures of T and T + ΔT, respectively. For the uniform detector,

$$SNR_{1-x} = D^* (1 - x) P_d(T) / [(1 - x) A_d \Delta f]^{\frac{1}{2}} ,$$

$$SNR_x = D^* x P_d(T+\Delta T) / [x A_d \Delta f]^{\frac{1}{2}} ,$$

whereas for the non-uniform detector

$$SNR'_{1-x} = D^* (1 - x) P_d(T) / [(1 - x) A_d \Delta f]^{\frac{1}{2}} ,$$

$$SNR'_x = (1 + d) D^* x P_d(T+\Delta T) / [x A_d \Delta f]^{\frac{1}{2}} .$$

Here P_d denotes the power incident upon the detector, and is given by

$$P_d = B_\nu (T) \Delta\nu \; A_o \tau_o \Omega .$$

The combined signal to noise ratio is

$$SNR = (S_{1-x} + S_x) / (N_{1-x}^2 + N_x^2)^{\frac{1}{2}} .$$

However, it is reasonable to assume that the noise contributions are proportional to the areas, so

$$N_{1-x} / N_x = (1-x) / x .$$

Thus,

$$SNR = [(1-x)\ SNR_{1-x} + x\ SNR_{x}] / [x^2 + (1-x)^2]^{\frac{1}{2}} \quad .$$

Since SNR_{1-x} is the same for both the uniform and non-uniform detectors, it follows that

$$SNR' - SNR = ([x^{3/2}\ d / [x^2 + (1-x)^2]^{\frac{1}{2}})\ D^*\ P_d(T+\Delta T) / [A_d\ \Delta f]^{\frac{1}{2}} \quad .$$

Thus, the value of d which leads to a difference of one in the signal to noise ratios is

$$d = ([x^2 + (1-x)^2]^{\frac{1}{2}} / x^{3/2}) / (D^*\ P_d(T+\Delta T) / [A_d\ \Delta f]^{\frac{1}{2}}) \quad .$$

For illustration, consider channel 1 of the sounder.

ν	=	690	cm^{-1}
$\Delta\nu$	=	12	cm^{-1}
T	=	240	K
Δf	=	35	Hz
A_d	=	250	μm
D*	=	1×10^{10}	$W^{-1}\ cm\ Hz^{\frac{1}{2}}$
τ_o	=	0.3	
$\Delta\theta$	=	224	μrad

Then

$$219.4\ d = [x^2 + (1-x)^2]^{\frac{1}{2}} / x^{3/2} \quad .$$

This curve is plotted in Figure 20. It is clear that only gross non-uniformities can cause a problem if x is less than 1%. Conversely, if d = 5% is the best uniformity available, then the area of such hot spots should not exceed 18%.

APPENDIX 7. Radiant cooler design.

The radiant cooler consists of three stages:

(1) the 'patch' at temperature T_p = 100 K, which allows a 5 K margin so that the patch can be regulated to an operating temperature of 105 K;

(2) a 'radiator' at temperature T_r = 150 K;

(3) a sun shield at temperature T_s = 240 K.

The temperature of the instrument housing (T_h) is assumed to be 290 K.

The thermal balance equation for the cooler is

$$F_p = F_d + F_k + F_c + F_a + F_s + F_o \quad ,$$

where the subscripts have the following meanings:

p : patch

d : detector dissipation

k : conductance (mechanical and electrical connections)

c : cavity radiation between the patch and radiator

a : non-specular scattering by the sun shield

s : sun shield

o : optical ports

In discussing each of these terms the emissivity of the black radiating side of surface x will be denoted by ε_{xb}, whereas the emissivity of the shiny (gold plated) reflecting surface will be denoted by ε_{xs}. The view factor of surface x from surface y is denoted by f_{xy}.

(1) F_p is the flux radiated by the patch,

$$F_p = \varepsilon_{pb} A_p \sigma T_p^4 \quad ,$$

where σ is the Stefan-Boltzmann constant.

(2) F_d is the power dissipation of the infrared detector arrays, detailed in the power budget calculations.

(3) F_k is the conductive heat load into the patch. It consists of two terms. The first, F_{kl}, represents conduction along the electrical leads to the detectors, heaters and sensors on the patch, and the second, F_{ks}, represents conduction through the mechanical supports for the patch.

In calculating F_{kl}, the leads have been reckoned as shown in Table 25.

TABLE 25. Electrical leads into the patch.

Instrument	Component	#	@	total
Sounder	PC detectors	32	2 leads/detector	64
Sounder	PV detectors	40	1 lead /detector	40
Sounder	PV arrays	2	1 lead /array	2
Imager	PC detectors	32	2 leads/detector	64
Imager	PV detectors	48	1 lead /detector	48
Imager	PV arrays	3	1 lead /array	3
Window heater		1	2 leads	2
Patch thermostat heater		1	2 leads	2
Patch thermostat sensor		1	2 leads	2
Outgas heater		1	2 leads	2
				229

The leads were assumed to be ribbon cable wrapped around a 150 mm support post. The material was assumed to be Ni with

thermal conductivity	k_l = 128	$Wm^{-1}\ K^{-1}$	
diameter	d_l = 37.5	μm	
length	l_l = 375	mm	

Then

$$F_{kl} = n\, k_l\, A_l\, l_l^{-1}\, (T_r - T_p) \quad ,$$

$$= 8.633 \times 10^{-5}\, (T_r - T_p) \quad .$$

The heat conducted to the patch from the radiator through the supports is estimated to be

$$F_{ks} = k_s\, A_p\, l_s^{-1}\, (T_r - T_p) \quad ,$$

where

post conductivity $k_s = 5.3\times10^{-4}$ $Wm^{-1}\ K^{-1}$,

post length $l_s = 150$ mm .

The value of k_s assumes fibre epoxy hollow tubes (synthane G-10), such as used on the AVHRR instrument, and is scaled according to the patch area because the larger the patch the greater will be the number of supports required.

$$F_{ks} = 3.533\times10^{-3}\ A_p\ (T_r - T_p) \quad .$$

(4) F_c represents the flux radiated to the gold plated underside of the patch by the gold plated topside of the radiator.

$$F_c = 2\ (\varepsilon_{ps}^{-1} + \varepsilon_{rs}^{-1} - 1)^{-1}\ A_p\ \sigma\ (T_r^4 - T_p^4) \quad .$$

(5) F_a represents the flux due to non-specular reflection from the sun shield. The precise value of F_a is difficult to obtain, because it depends on both the material and geometry of the sun shield, so a value of 30 mW has been assumed.

(6) F_s denotes the sun shield to patch radiant emission.

$$F_s = \varepsilon_{ss}\ \varepsilon_{pb}\ f_{ps}\ A_p\ \sigma\ T_s^4 \quad .$$

(7) F_o is the thermal flux transmitted through the optical ports in the housing and radiator into the patch. F_o consists of two terms,

$$F_o = F_{oh} + F_{or} \quad .$$

The first term is the flux from the housing window onto the patch,

$$F_{oh} = \tau_r\ \varepsilon_{hb}\ \varepsilon_{pb}\ f_{ph}\ A_p\ \sigma\ T_h^4\ \eta(T_h, \lambda_0, \lambda_1) \quad ,$$

where (λ_0, λ_1) is the bandpass of the port and η is the band-pass factor for radiation at temperature T_h,

$$\eta(T, \lambda_0\lambda_1) = \pi \int_{\lambda_0}^{\lambda_1} B_\lambda(T)\ d\lambda\ /\ \sigma\ T^4 \quad .$$

The second term is the flux radiated from the radiator window to the patch plus half the radiation within the cavity between the radiator and patch,

$$F_{or} = \varepsilon_{rb}\,\varepsilon_{pb}\,f_{pr}\,A_p\,\sigma\,T_r^4\,\eta\,(T_r, \lambda_0, \lambda_1)$$

$$+ \tfrac{1}{2}\,\varepsilon_{rb}\,(1-f_{rp})\,A_r\,\sigma\,T_r^4 \quad .$$

The view factor for discs of radii r_1 and r_2, separated by a distance h, is

$$f_{12} = \tfrac{1}{2}\,[\,x - \sqrt{x^2-4R_2^2/R_1^2}\,] \quad ,$$

where

$$x = 1 + \frac{1+R_2^2}{R_1^2} \quad , \quad R_1 = \frac{r_1}{h} \quad , \quad R_2 = \frac{r_2}{h} \quad .$$

There are 8 ports into the patch whose radii are listed in Table 26. The values used for the various parameters are:

$T_p = 100$ K
$T_r = 150$ K
$T_h = 290$ K
$T_s = 240$ K
$\varepsilon_{pb} = 0.970$
$\varepsilon_{rb} = 0.900$
$\varepsilon_{hb} = 0.900$
$\tau_r = 0.95$
$f_{ps} = 0.60$
$\varepsilon_{ps} = 0.031$
$\varepsilon_{rs} = 0.035$
$\varepsilon_{ss} = 0.011$

TABLE 26. Optical ports into the patch.

Instrument	Channel	Patch port radius	Angular field of view
Sounder	shortwave	2.7 mm	25°
	mediumwave	1.0 mm	25°
	longwave	2.5 mm	25°
Imager	5 channels	0.5 mm	20°